Brief Review

Modern Physics Letters B, Vol. 21, No. 21 (2007) 1357–1376

World Scientific
www.worldscientific.com

SHEAR VISCOSITY OF STRONGLY-COUPLED TWO-DIMENSIONAL YUKAWA LIQUIDS: EXPERIMENT AND MODELING

Z. DONKÓ and P. HARTMANN

Research Institute for Solid State Physics and Optics of the Hungarian Academy of Sciences, H-1525 Budapest, P.O. Box 49, Hungary

J. GOREE

Department of Physics and Astronomy, The University of Iowa, Iowa City, Iowa 52242, USA

Received 31 July 2007

This paper reviews experimental and modeling efforts aimed at the determination of the shear viscosity of strongly-coupled Yukawa liquids. After briefly reviewing prior work on three-dimensional (3D) systems, recent experimental and computer simulation studies of two-dimensional (2D) settings are presented in detail. In the experiments two counterpropagating laser beams were used to perturb a dusty plasma monolayer and monitoring of the velocity field reconstructed from particle trajectories allowed the determination of the shear viscosity with the aid of an analytical model. Subsequent computer simulations based on the molecular dynamics approach resulted in velocity profiles which are in very good agreement with the experimental ones. Further simulation studies of idealized 2D Yukawa liquids (in which gas friction is neglected) gave results for the shear viscosity over a wide range of system parameters and demonstrated the existence of the shear thinning effect (non-Newtonian behavior) of the liquid at high shear rates.

Keywords: Strongly-coupled plasma; Yukawa liquid; shear viscosity.

1. Introduction: General Characteristics of Yukawa Liquids

Strongly-coupled plasmas — in which the average interaction (potential) energy per particle dominates over the average kinetic energy — appear in a wide variety of physical systems: dusty plasmas, charged particles in cryogenic traps, condensed matter systems such as molten salts and liquid metals, electrons trapped on the surface of liquid helium, astrophysical systems, such as the ion liquids in white dwarf interiors, neutron star crusts, supernova cores, and giant planetary interiors, as well as in degenerate electron or hole liquids in two-dimensional or layered semiconductor nanostructures.[1]

Many of the systems listed above can be described in terms of classical physics and share some properties, which allows one to describe them by the *one-component*

plasma (OCP) model. The OCP model considers explicitly only a single type of charged species and uses a potential that accounts for the presence and effects of other types of species. This latter may be considered as a charge-neutralizing background, which is either non-polarizable or polarizable. In the first case the *pair interaction energy* of the main plasma constituents is Coulombic:

$$\phi(r) = \frac{Q^2}{4\pi\varepsilon_0}\frac{1}{r}\,, \tag{1}$$

whereas in the case of polarizable background, screening effects can be accounted for by the

$$\phi(r) = \frac{Q^2}{4\pi\varepsilon_0}\frac{\exp(-r/\lambda_\mathrm{D})}{r} \tag{2}$$

Yukawa potential (Q is the charge of the particles and λ_D is the Debye length). The Yukawa potential is applicable, in particular, for dusty plasmas[2–6] and charged colloids.[7–10]

It is conventional to express the ratio of the interparticle potential energy to thermal energy by the *coupling parameter*:

$$\Gamma = \frac{Q^2}{4\pi\varepsilon_0}\frac{1}{ak_\mathrm{B}T}\,, \tag{3}$$

where a is the Wigner–Seitz (WS) radius, and T is the temperature. Depending on whether the system is three-dimensional or two-dimensional, a is defined as $(3/4\pi n)^{1/3}$ or $(n\pi)^{-1/2}$, respectively, where n is the volume or areal number density. The strong coupling regime corresponds to $\Gamma \gg 1$.

In the case of Yukawa interaction an additional essential parameter is the *screening parameter*:

$$\kappa = \frac{a}{\lambda_\mathrm{D}}\,. \tag{4}$$

In Eqs. (3) and (4), we use as the length scale a the Wigner–Seitz radius, although some authors use other length scales. In the $\kappa \to 0$ limit the interaction reduces to Coulomb type, while at $\kappa \to \infty$ it approximates the properties of a hard sphere system.

The liquid state, which is our focus in this review, occurs at coupling parameters $\Gamma > \Gamma_m$, where the melting point has been found in simulations to be $\Gamma_m \cong 175$ in 3D[11,12] and $\Gamma_m \cong 137$ in 2D,[13,14] both for the Coulomb limit $\kappa = 0$. In a Yukawa system, Γ_m increases with κ, for both 3D[15] and 2D[16,17] systems.

Complex (dusty) plasmas — which are of special interest here – can be created in laboratory experiments by dispersing micron-sized particles into gas discharges.[18] The (typically noble gas) glow discharge can be direct current (d.c.) or radio-frequency (r.f.) driven and serves primarily as a charging medium for the (typically spherical, dielectric) particles. The dust particles are exposed to electron and ion currents from the discharge plasma, and a dynamic equilibrium is

rapidly reached, where their net electric charge can be in the order of $\sim 10^4$ electron charges. These particles interact with their environment with several forces: gravity (which is proportional to the mass of the particle), ion drag force, neutral drag force, and thermophoretic forces (which are all proportional to the particle's surface area), and the Coulomb force (which is proportional to charge and therefore the particle radius). The dominance of the different force contributions can be tuned by adjusting the experimental conditions, including particle size. In this paper we focus our attention on systems where the particles are levitated in a horizontal plane-parallel electrode configuration r.f. discharge. In this case gravity is compensated by the Coulomb force arising from the vertical electric field of the plasma sheath, and the particles settle in a single 2D layer near the lower electrode. If more particles were added, additional layers would form, but in the experiments described here the particle number is limited to allow only a single layer to form. This configuration allows a simplified analysis because ion drag forces act mainly perpendicular to the particle plane, therefore they influence only the equilibrium position of this layer. In this configuration, the interparticle potential can be well approximated by a simple Yukawa type interaction, originating from the Coulomb repulsion of the charged dust particles and the polarizability (screening property) of the surrounding discharge plasma.

Transport properties of strongly-coupled plasmas in the *liquid state* have attracted considerable interest since the 1970s. Among the transport parameters *shear viscosity* is the focus of the present paper. Transport coefficients are meaningful if they are part of a valid "constitutive relation" between the gradients of local variables and fluxes. For shear viscosity η, the constitutive relation

$$j_y = -\eta \frac{dv_x(y)}{dy} \tag{5}$$

relates the "transverse" momentum flux j_y to the velocity gradient $dv_x(y)/dy$, which is also termed the shear rate. In a *non-Newtonian* fluid, η may vary with the velocity gradient, whereas in *Newtonian* fluids it does not. In particular, if η diminishes as shear is increased, the fluid is said to exhibit "shear thinning". Following the studies on simple liquids by Evans and co-workers,[19] such behavior has been receiving increasing interest during the last couple of years, as many different systems have been found to exhibit such features. Examples of such systems include complex mixtures such as foams, micelles, slurries, pastes, gels, polymer solutions, and granular flows.[20] Recently, the possibility of shear thinning in dusty plasmas has attracted the attention of experimenters.[21,22]

In addition to non-Newtonian effects such as shear thinning, there is another reason that the constitutive relation, Eq. (5), can fail. This failure arises from the discrete nature of particles.[23] If a shear layer is so narrow that there are only a few molecules or particles across its width, the particles cannot be modeled as a continuum, with a fluid velocity v.

In Sec. 2 we briefly summarize previous work related to the shear viscosity of 3D Coulomb and Yukawa liquids. In Secs. 3 and 4 we turn to 2D liquids, where there are not only recent simulations but also experimental efforts aimed at determining the shear viscosity.

2. Prior Work on Shear Viscosity of 3D Coulomb and Yukawa Plasma Liquids

The shear viscosity of 3D Coulomb and Yukawa liquids has been investigated by several authors. Calculated viscosity values obtained in earlier studies for $\kappa \cong 0$ and $\kappa = 1$, respectively, are displayed in Figs. 1(a) and 1(b), as a function of the coupling parameter Γ. The data are normalized by $\eta_0 = mn\omega_0 a^2$ where m is the mass of the particles, n is the particle density, $\omega_0 = \sqrt{Q^2 n/\epsilon_0 m}$ is the plasma frequency, and a is the Wigner–Seitz radius, $a = (3/4\pi n)^{1/3}$.

Regarding Coulomb systems, the shear (η) and bulk (ζ) viscosity of the 3D OCP was first derived by Vieillefosse and Hansen[24] from the transverse and longitudinal current correlation functions of the plasma. They found that the shear viscosity exhibits a minimum at $\Gamma \approx 20$. The calculations of Wallenborn and Baus[25,26] were based on the kinetic theory of the OCP; their results were in a factor of three agreement with the previous results[24] at $\Gamma = 1$ and within a factor of two agreement at $\Gamma = 160$. The minimum value of η agreed well for both reports, however the position of the minimum was reported in the latter work to occur at a lower coupling value, $\Gamma \approx 8$.[25] Molecular dynamics simulation was first applied by Bernu, Vieillefosse and Hansen[27,28] to obtain transport parameters through the Green–Kubo relations. Donkó and Nyíri[29] used a nonequilibrium MD simulation

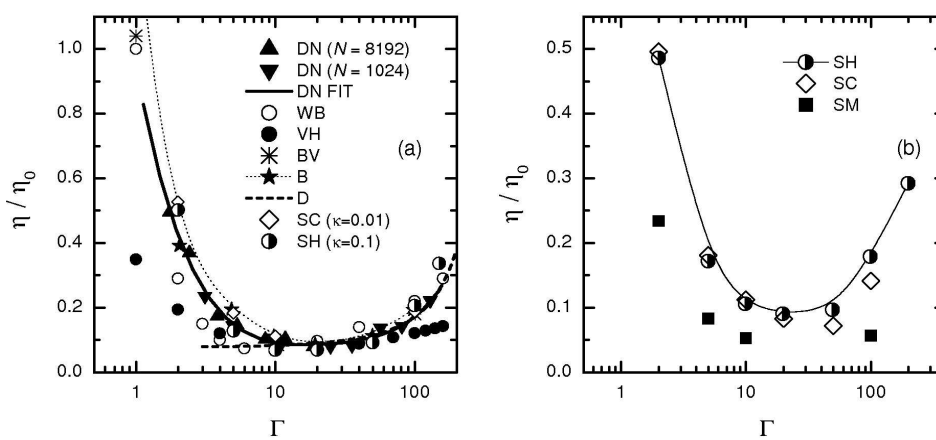

Fig. 1. Shear viscosity coefficient of the 3D classical one-component plasma (OCP) normalized by $\eta_0 = mn\omega_0 a^2$ (see text). (a) Coulomb liquids ($\kappa = 0$) and Yukawa liquids with $\kappa \cong 0$. (b) Yukawa liquids with $\kappa = 1$. DN: Donkó and Nyíri[29] using 1024 and 8192 particles, WB: Wallenborn and Baus,[25,26] VH: Vieillefosse and Hansen,[24] BV: Bernu *et al.*,[27,28] B: Bastea,[30] D: Daligault,[31] SC: Salin and Caillol,[32] SH: Saigo and Hamaguchi,[33] Sanbonmatsu and Murillo.[23]

technique to determine the shear viscosity, while subsequently, Bastea[30] applied equilibrium simulation to obtain η for 3D Coulomb liquids using the Green–Kubo relation. Recently Daligault found that the shear viscosity of the OCP follows an Arrhenius type behavior at high Γ values.[31] (These latter results have been scaled by us in Fig. 1(a) so that they match the minimum value of η, given by the other calculations.)

Concerning Yukawa systems, Salin and Caillol[32] have carried out equilibrium molecular dynamics computations for the shear and bulk viscosity coefficients, as well as for the thermal conductivity. Saigo and Hamaguchi[33] have also used the Green–Kubo relations for the calculations of the shear viscosity. Sanbonmatsu and Murillo[23] calculated the shear viscosity from nonequilibrium MD simulations (which apply a spatial velocity profile perturbation). Murillo[34] and later on Faussurier and Murillo[35] obtained transport coefficients through mapping of the Yukawa liquid and hard sphere, as well as one-component Coulomb systems.

As opposed to simple liquids, it is a remarkable feature of the $\eta(\Gamma)$ graphs that they exhibit a minimum at intermediate values of the coupling coefficient. The shape of the $\eta(\Gamma)$ curves can be explained by the prevailing potential and kinetic contributions to the viscosity at low and high values of Γ, respectively.[33] Comparing the results shown in Figs. 1(a) and 1(b) we can observe that with increasing screening (i.e. increasing κ) the minimum of the $\eta(\Gamma)$ curve is shifted towards higher Γ.

When, however, Saigo and Hamaguchi[33] normalized their results by $\eta_0' = mn\omega_{\mathrm{E}}a^2$ (where ω_{E} is the Einstein frequency) and plotted these against the normalized temperature $T' = T/T_{\mathrm{m}}$, they found that the viscosity obeys a universal, κ-independent scaling $\eta/\eta_0' = aT' + b/T' + c$ (a, b, and c are constant coefficients). The Einstein frequency ω_{E} which appears above is defined as the oscillation frequency of a test particle in the frozen environment of the other particles,[33,36] while T_{m} is the melting temperature. Here, T_{m} and ω_{E} are κ-dependent. It has been demonstrated[16] that for many dynamical processes, ω_{E} provides a more appropriate normalization of time than the κ-independent plasma frequency.

3. Dusty Plasma Shear Viscosity Experiment

Next we turn our attention to two-dimensional Yukawa liquids, where there are not only simulations, but also experiments. Moreover, these simulations and experiments are well suited to a direct comparison. Here we will normalize time using either the 2D analog of the plasma frequency $\omega_0 = (Q^2/2\pi\varepsilon_0 ma^3)^{1/2}$, or the Einstein frequency ω_{E}. We will normalize distances by $a = 1/\sqrt{n\pi}$, the 2D Wigner–Seitz radius, where n is the areal density.

Experiments are performed using low-pressure gaseous discharges in the way already explained in Sec. 1. To investigate viscosity, a sheared velocity profile has to be established; in the experiments of Nosenko and Goree[37] this was accomplished by directing two parallel, but counterpropagating laser beams onto the particle

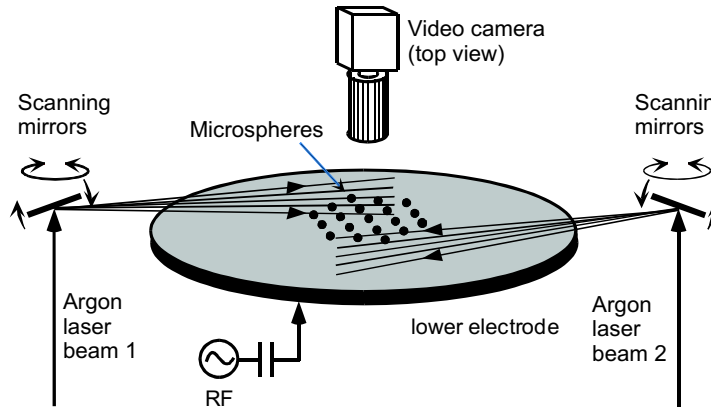

Fig. 2. Sketch of experimental apparatus.

suspension. The experimental apparatus is sketched in Fig. 2. A vacuum chamber, not shown in Fig. 2, is filled at a low pressure with an inert gas to allow the production of a glow-discharge plasma when radio-frequency voltages are applied to electrodes. A horizontal lower electrode is powered through a capacitor, so that a negative d.c. bias can develop naturally on this electrode. The entire vacuum chamber serves as the other electrode. Polymer microspheres are dispensed with a simple device like a salt shaker so that they fall into the plasma, where they become negatively changed. They are levitated in a high electric field region above the negatively-biased lower electrode. Due to their great inertia, these dust particles respond only to d.c. fields, and not to the radio-frequency fields which are used to accelerate electrons and sustain the ionization of the plasma.

The gas in the vacuum chamber is only partially ionized, so that particles experience a frictional force as they move through the gas. This force is proportional to the particle velocity, with a known coefficient.[38] Unlike 3D particle suspensions, the particles in the 2D suspension are too few for their mass motion to cause a flow in the gas.

The particles are imaged by illuminating them with a low-power laser beam dispersed into a horizontal sheet, and images are recorded by a video camera and a digital VCR. Particle positions are measured in each video frame using a moment method, and particles are tracked between two consecutive frames to allow a calculation of the velocity of each particle that is imaged. The camera operated at 30 frames per second, with a 23.1×17.3 mm field of view that included 370–770 particles.

A single layer of microspheres was suspended in the plasma. The particles had a diameter[38] of 8.09 ± 0.18 μm and a mass $m = 4.2 \times 10^{-13}$ kg. The particle suspension's diameter was 50–60 mm. The interparticle potential for particles arranged in a single plane was experimentally shown[39] to be nearly of the form as given by Eq. (2).

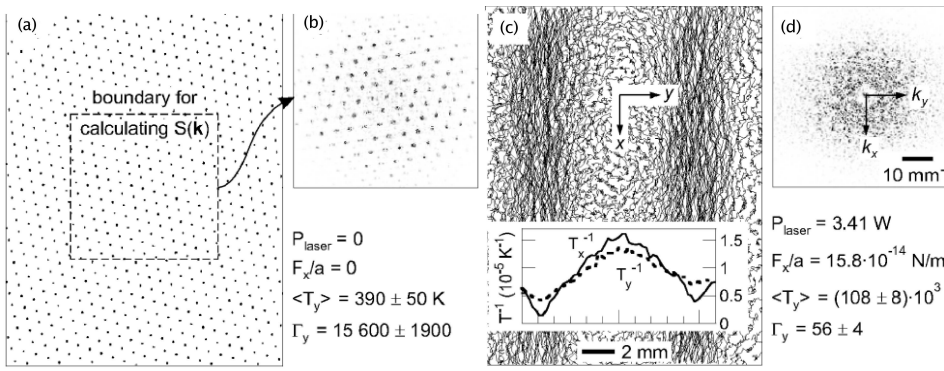

Fig. 3. A bitmap image of the central portion of the particle suspension shows the particles (a) and the structure factor $S(k)$ (b), both before the manipulation lasers are applied to produce a shear stress. The particles are arranged in a crystalline triangular lattice with hexagonal symmetry. Results during steady-state application of shear stress using a pair of counterpropagating laser beams are shown as particle trajectories (c) and $S(k)$ (d), for a steady-state shear flow. Profiles of the inverse particle temperature T_x^{-1} and T_y^{-1} are shown in the insets. The static structure factor $S(\mathbf{k})$ was computed as the Fourier transform of the raw bitmap images as in (a). (Adapted from Ref. 37. Copyright (2004) by the American Physical Society.)

Initially the suspension was an undisturbed triangular lattice, see Fig. 3(a), in a highly ordered state. The static structure factor $S(\mathbf{k})$ had the distinctive peaks of a hexagonal crystal, Fig. 3(b).

Particles were manipulated by applying a pair of powerful cw laser beams. The powers of these two beams were nearly the same, and they could be varied over a range of a few Watts, as measured inside the vacuum chamber. These laser beams apply a radiation-pressure force to particles that are struck by the laser; this force is proportional to the applied laser intensity.[38] To apply a shear stress, the two laser beams were applied in a counterpropagating configuration.

Beginning with an undisturbed lattice, the laser beams were then turned on to apply a shear stress, causing the particle suspension to melt and develop a steady-state shear flow. The camera field of view shows only a central portion of the entire flow pattern, which was a pair of counter-rotation vortices. At their junction, where the camera's field of view was located, this pair of vortices made a shear flow with a nearly one-dimensional symmetry. More than 95% of the time-averaged flow velocity was directed in the x-direction, with less than 5% of the flow velocity diverted in the y-direction. The flow velocity varied little with x within the field of view, so that the flow can be modeled as a one-dimensional shear flow.

Particle velocities were averaged within bins, yielding v_x and v_y as a function of y. Likewise, the mean-square fluctuations of particle velocity were computed to yield the kinetic temperature $T_x(y)$ and $T_y(y)$. Profiles of the temperature are shown in Fig. 3(c), while the velocity profile, which is one of the chief experimental results, is shown in Fig. 4.

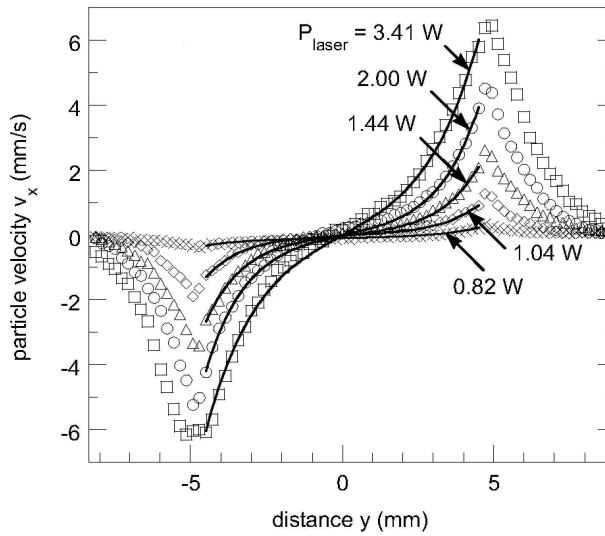

Fig. 4. Experimental particle velocity profiles (data points) are shown with fits to the Navier–Stokes model (curves) for various laser powers. (Adapted from Ref. 37. Copyright (2004) by the American Physical Society.)

The flow velocity profile $v_x(y)$ in Fig. 4 was curved, unlike in a traditional planar Couette flow where $v_x(y)$ is linear with y. This curvature can be attributed to the frictional drag exerted on particles by the gas. A balance between this drag in the x direction and the viscous transport of particle momentum in the y direction away from the laser stripes accounts for the observed steady-state velocity profile.

The velocity profile was modeled in the continuum approximation, using the Navier–Stokes equation, which includes a viscous term corresponding to the constitutive relation for viscosity (Eq. (5)). Also added to the Navier–Stokes equation, especially to model this experiment, is a final term for the gas drag

$$\frac{\partial \mathbf{v}}{\partial t} + (\mathbf{v}\nabla)\mathbf{v} = -\rho^{-1}\nabla p + \frac{\eta}{\rho}\nabla^2\mathbf{v} + \left[\frac{\zeta}{\rho} + \frac{\eta}{3\rho}\right]\nabla(\nabla\cdot\mathbf{v}) - \nu_d\mathbf{v}. \tag{6}$$

Here, the parameters for the continuum representing the particle suspension are $\mathbf{v}$, p, ρ, η, and ζ, which are the velocity, pressure, areal mass density, shear (dynamic) viscosity, and second viscosity, respectively, and ν_d is the gas friction. The ratio η/ρ is the kinematic viscosity, which has the same dimensions in 2D and 3D systems. The flow has a symmetry $\partial/\partial x = 0$ and $v_y = 0$. The Navier–Stokes equation is then reduced to

$$\frac{\partial^2 v_x(y)}{\partial y^2} - \frac{\nu_d\rho}{\eta}v_x(y) = 0, \tag{7}$$

and $p = \text{const}$. Solving Eq. (7) yields a theoretical velocity profile

$$v_x^{th}(y) = \frac{(V_1 + V_2\,\mathrm{e}^{2\alpha h})\mathrm{e}^{\alpha y} - (V_2 + V_1\,\mathrm{e}^{2\alpha h})\mathrm{e}^{-\alpha y}}{\mathrm{e}^{3\alpha h} - \mathrm{e}^{-\alpha h}}, \tag{8}$$

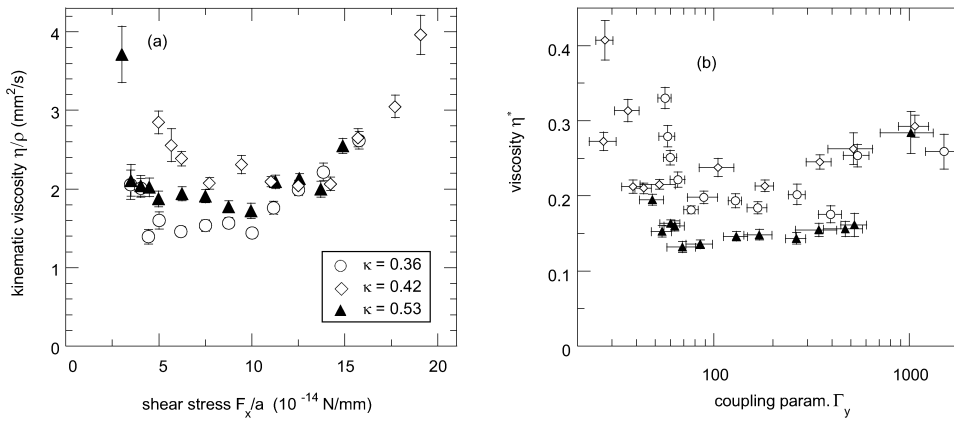

Fig. 5. Results for kinematic viscosity η/ρ, as a functions of the shear stress (a) and temperature (b). There is a broad minimum in viscosity in the range $70 < \Gamma_y < 700$. In (b), to allow comparison to theory, the viscosity is normalized by $\eta_0 = mn\omega_0 a^2$, as usual. (Adapted from Ref. 37. Copyright (2004) by the American Physical Society.)

where $\alpha = \sqrt{\nu_d\,\rho/\eta}$ and $2h$ is the distance between the laser sheets. The boundary conditions $v_x(-h) = -V_1$ and $v_x(h) = V_2$ are used, where V_1 and V_2 are the observed peak velocities in the laser stripes.

Here the spatial dependence of η/ρ is ignored, thereby neglecting the temperature gradient in the shear flow. The presence of a significant temperature gradient, with a variation of temperature over a factor of three within the observed region, will somewhat limit the accuracy of the determination of the viscosity coefficient to an extent that may require future experiments to quantify.

To find the viscosity, the experimental velocity profiles in Fig. 4 are fitted to theory using experimental values of V_1 and V_2 and a single free parameter α. The resulting curves fit the experimental profiles well. Using the known value of Epstein gas drag $\nu_d = 0.87\ \mathrm{s}^{-1}$ for the experimental conditions,[38] the kinematic viscosity was calculated as

$$\frac{\eta}{\rho} = \nu_d\,\alpha^{-2}. \tag{9}$$

The main experimental result was the kinematic viscosity η/ρ of the particle suspension, Fig. 5(a). Its value is of order 1 $\mathrm{mm}^2\mathrm{s}^{-1}$, which is comparable to η/ρ for both a 3D Yukawa system and liquid water.[23,32,33,35,40] For a given value of κ, the parameter varied was the applied laser power; increasing this power caused the shear stress to increase and Γ_y to decrease, so that these two parameters were not varied independently.

A prominent feature of Figs. 5(a) and 5(b) is a broad minimum in the viscosity. The minimum occurs in the range $70 < \Gamma_y < 700$. This minimum is generally similar to the minimum found in simulations of 3D Yukawa liquids.[23,32,33,35]

Having a value for the viscosity allows an estimate of the Reynolds number R of the shear flow. This dimensional ratio indicates whether a flow is viscous or turbulent. For this experiment, $R = V_1 h/(\eta/\rho) = 0.7$–$17$; values this low indicate a laminar flow, validating that assumption in using a simplified Navier–Stokes equation (Eq. (7)).

The good fit in Fig. 4 suggests that the Navier–Stokes model, which is a continuum model that does not describe motion of individual molecules, works well even when the ratio of the shearing region width $2h$ to the Wigner–Seitz radius a is as small as 17 to 24, as it was in the experiment. Although the results indicate that the shearing region had a sufficient width to use the Navier–Stokes equation, the laser stripes are surely too narrow, because they were less than an interparticle spacing in breadth. Thus, the Navier–Stokes equation was applied only in the shearing region and not in the narrower laser stripes. In general, if the continuum approximation underlying the Navier–Stokes equation fails to apply, one cannot expect the constitutive relation for viscosity to hold.

4. Simulations

In this section we introduce the basic concepts of molecular dynamics (MD) simulations. Subsequently, in Sec. 4.1 we describe a simulation using experimental parameters matching those of the previous section. Finally we describe idealized equilibrium and non-equilibrium simulations in Secs. 4.2 and 4.3 for frictionless systems, unlike the experiment.

Molecular dynamics simulations follow the motion of particles by integrating their equations of motion while accounting for the pairwise interaction of the particles.[41] The Newtonian equation of motion that is integrated is simply

$$m\ddot{\mathbf{r}}_i = \mathbf{F}_i, \tag{10}$$

where $\mathbf{F}_i$ is the total force acting on particle i due to all the other particles and due to any other forces, due for example to externally-applied electric forces, laser radiation pressure, or gas friction. The way $\mathbf{F}_i$ is calculated will be discussed below.

MD simulations in general can have either periodic boundary conditions to simulate an infinite system, or they can have boundaries to simulate every particle in a finite system. Here we use periodic boundary conditions, where a particle exiting one side of the simulation box re-enters the opposite side. Particles interact not only with other particles in the simulation box, but also particles in image boxes. In this way, finite computational resources can be used to mimic an infinite system.

The interparticle forces can be calculated either by a simple pairwise particle–particle (PP) method, or a more complicated method, depending on the range of the potentials. The easier case, which we report in the following sections, is for relatively short-range potentials, where it is possible to limit the number N^2 of pairwise interactions that are included by using a truncation of the potential.

A common method of doing this is to apply a cutoff radius, beyond which any interparticle interactions are neglected. For a Yukawa system, this cutoff radius is typically a multiple of λ_D. The more difficult case is for longer-range potentials, such as the unshielded $1/r$ Coulomb potential for OCP systems, which does not allow a simple truncation of the potential. For those systems, which are not modeled in the following section, it is typical to use either Ewald summation,[42] the fast multipole method, or the particle–particle particle–mesh method (PPPM, or P3M).[43–47] The authors have previously used the PPPM method to model OCP systems, but for the finite κ Yukawa systems modeled here a simpler truncation of the potential is used.

At the initialization of the simulations usually a random particle configuration is set up, with velocities sampled from a Maxwellian distribution of temperature T_0, which corresponds to the desired value of the coupling parameter Γ (see Eq. (3)). The equations of motion of the particles are integrated using the leapfrog scheme or the velocity-Verlet scheme. The desired system temperature is reached by rescaling the particle momenta during an initialization phase of the simulation. The desired measurements are made after this initialization phase.

Molecular dynamics simulations provide two basic ways for the determination of transport coefficients. In non-equilibrium simulation methods an external perturbation is applied to the system and the system's response (linked to the perturbation through a transport coefficient) is measured and compared to the constitutive relation. In equilibrium simulations, no perturbation is applied because the system is intended to mimic a thermodynamic equilibrium. Consequently, there is no gradient, and the constitutive relation is not used. To find macroscopic transport coefficients using an equilibrium code, one uses the Green–Kubo (GK) relations, which require a calculation of correlation functions of microscopic quantities such as particle velocity. In equilibrium simulations, some workers use thermostats (like the Nosé–Hoover thermostat[41]) throughout the simulation to maintain a desired temperature, while others do not.

In the following sections first we present the molecular dynamics simulation of the experiment discussed in Sec. 3. Subsequently, in Secs. 4.2 and 4.3, MD simulations aimed at the determination of idealized (frictionless) 2D Yukawa liquids are presented and discussed.

4.1. *Simulation of the experiment*

To model the shear flow dusty plasma experiment, we adapted an equilibrium MD code to include not only interparticle forces, but also two additional terms in the equation of motion: the gas friction and laser radiation pressure forces. The gas friction force is $-\nu_d \mathbf{v}$. The laser radiation-pressure force, which is localized to two stripes as in the experiment, is proportional to the laser intensity, which has a Gaussian profile $I = I_0 \exp(-2r^2/w^2)$. Here, the coordinate r is the distance from the laser beam center and for the width of the beams we use the experimental value $2w = 0.61$ mm.

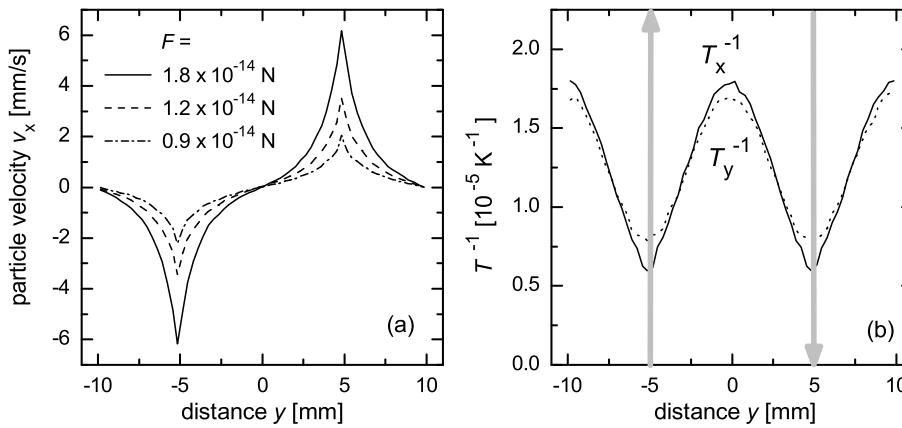

Fig. 6. Velocity (a) and inverse temperature (b) profiles obtained in the simulation of the dusty plasma experiments. The labels of the curves indicate the values of the external force acting on the particles in the beam waist of the laser. The gray arrows in (b) indicate the laser stripe locations.

In the MD simulation we used $N = 757$ particles arranged in a rectangular simulation box fitting the shape of the observation region in the center of the experiment. The simulated system is intended to model the camera's field of view in the experiment. By using periodic boundary conditions, it was not necessary to model the portions of the experimental suspension that were not in the field of view; those portions include a pair of counter-rotating vortices driven by the shear applied in the field of view.

In the absence of laser beams the simulated system crystallizes due to the continuous cooling by the neutral drag. Following the initialization of the simulation, and having the laser beams "turned on", ample time was given to the system to reach a stationary state, and sampling of the particle velocity profiles starts afterwards. The simulations have been carried out using different laser intensities; a series of results is presented in Fig. 6. The force values indicated in Fig. 6 were adjusted to achieve peak velocities matching those observed in the experiment; this force does not necessarily match the experimental force because in the experiment the lasers pushed a flow of a larger number of particles, due to the particles outside the observation region. It is only the observation region that is modeled by the simulation box, which uses periodic boundary conditions.

The results of this simulation are velocity and temperature profiles, Fig. 6, which appear very similar to those obtained in the experiment, as seen in Figs. 3 and 4. The velocity profiles are curved, and not straight as in the classical Couette flow, due to the gas friction. The temperature profiles are peaked in the laser stripes where the velocities are highest because energy deposition by the laser is localized there, while energy is lost throughout the system due to gas friction.

4.2. *Equilibrium molecular dynamics simulations of frictionless systems*

Equilibrium simulations for the determination of the shear viscosity coefficient are based on the Green–Kubo (GK) relation[48]

$$\eta = \frac{1}{VkT}\int_0^\infty \langle P^{xy}(t)P^{xy}(0)\rangle \mathrm{d}t, \tag{11}$$

where P^{xy} is the off-diagonal element of the pressure tensor:

$$P^{xy} = \sum_{i=1}^{N}\left[mv_{ix}v_{iy} - \frac{1}{2}\sum_{j\neq i}^{N}\frac{x_{ij}y_{ij}}{r_{ij}}\frac{\partial\phi(r_{ij})}{\partial r_{ij}}\right], \tag{12}$$

where N is the number of particles, and $r_{ij} = |\mathbf{r}_{ij}| = |\mathbf{r}_i - \mathbf{r}_j| = |(x_{ij}, y_{ij})|$.

A key issue in calculating transport coefficients using equilbrium simulations is determining whether the required correlation function decays fast enough for the GK integral to converge. Investigations of Alder and Wainwright concerning the slow ($\propto t^{-1}$) decay of the velocity autocorrelation function in two-dimensional systems, followed by subsequent simulation and theoretical studies have raised doubts that the integrals would converge and that any transport coefficient would be valid in two dimensions.[49,50] Recent studies[51,52] on 2D Yukawa liquids, however, indicate that the stress autocorrelation function $C_\lambda(t) = \langle P^{xy}(t)P^{xy}(0)\rangle$ decays faster than power law thus allowing its integration and determination of the shear viscosity through Eq. (11).

Results from two different MD equilibrium simulations, reported by Liu and Goree[51] using a thermostat and Donkó *et al.*[53] without a thermostat, will be presented in the next section together with results from non-equilibrium simulations.

4.3. *Non-equilibrium molecular dynamics simulations of frictionless systems*

In a non-equilibrium simulation, we apply a shear quantified by the shear rate $\gamma = dv_x/dy$, and its normalized value $\overline{\gamma} = (dv_x/dy)(a/v_0)$. This creates a gradient, which we then observe to determine the shear viscosity. Below, we will normalize quantities using the thermal velocity $v_0 = (2k_\mathrm{B}T/m)^{1/2}$, the 2D analog of the plasma frequency ω_0 or the Einstein frequency ω_E, and the Wigner–Seitz radius a.

We used two different techniques for non-equilibrium MD simulation, which we summarize below (see Fig. 7).

(i) *Reverse molecular dynamics method.* Here the cause-and-effect picture usually used in non-equilibrium molecular dynamics is reversed: the effect, the momentum flux, is imposed, and the cause, the velocity gradient (shear rate) is measured in the simulation.[54] The momentum in the liquid is introduced in a pair of narrow slabs A and B, which are situated at $y = L_y/4$ and $3L_y/4$, respectively. At regular time intervals τ we identify the particles in slabs A and B having

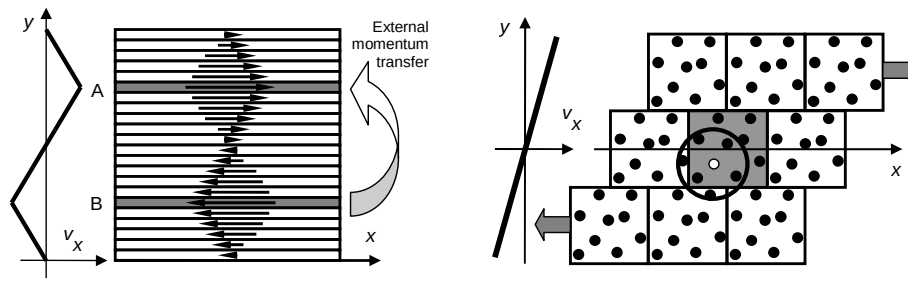

(a) (b)

Fig. 7. (a) Reverse molecular dynamics algorithm suggested by Müller-Plathe.[54] The artificially (externally) introduced momentum transfer between cells A and B is compensated by a momentum flux of opposite direction inside the liquid. The left part of the figure shows the $v_x(y)$ velocity profile that builds up in the system. The figure shows only the primary simulation box. Conventional periodic boundary conditions are applied. (b) Homogeneous shear algorithm, as described by Evans and Morriss,[55] based on the Lees–Edwards ("sliding brick") boundary conditions. The primary computational cell is shaded grey. "Upper" and "lower" images of this cell are moved with velocity $v = \pm\gamma(L_y/2)$, as indicated.

the highest $|v_x|$ in the positive and negative directions, respectively. We then instantaneously exchange the v_x velocity component of these two particles without moving the particles. This artificial transfer of momentum between slabs A and B (which is accomplished without changing the total energy of the system) creates a velocity profile $v_x(y)$. Unlike the scheme presented earlier to mimic the lasers in the experiment, here the shear is produced without introducing energy into the system. The slope of the resulting velocity profile, i.e., the shear rate γ, can be adjusted by controlling the frequency of the momentum exchange steps. The equations of motion are

$$\begin{aligned} \frac{d\mathbf{r}_i}{dt} &= \tfrac{\mathbf{p}_i}{m}\,, \\ \frac{d\mathbf{p}_i}{dt} &= \mathbf{F}_i\,, \end{aligned} \tag{13}$$

where $\mathbf{r} = (x, y), \mathbf{p} = (p_x, p_y)$ are the positions and the momenta of particles, m is their mass, and $\mathbf{F}_i$ is the force acting on particle i.

(ii) *Homogeneous shear algorithm.* As proposed by Evans and Morriss,[55] this technique uses the Lees–Edwards (sliding) periodic boundary conditions, as shown in Fig. 7(b). Here we obtain a homogeneous streaming flow field in the simulation box: $\langle v_x \rangle = \gamma(y - L_y/2)$, where $\langle\ \rangle$ denotes a time average. The system is described by the Gaussian thermostatted SLLOD equations of motion:[55]

$$\begin{aligned} \frac{d\mathbf{r}_i}{dt} &= \tfrac{\tilde{\mathbf{p}}_i}{m} + \gamma y_i \hat{\mathbf{x}}\,, \\ \frac{d\tilde{\mathbf{p}}_i}{dt} &= \mathbf{F}_i - \gamma \tilde{p}_{yi} \hat{\mathbf{x}} - \alpha \tilde{\mathbf{p}}_i\,, \end{aligned} \tag{14}$$

where $\tilde{\mathbf{p}} = (\tilde{p}_x, \tilde{p}_y)$ is the *peculiar* momentum of particles, $\hat{\mathbf{x}}$ is the unit vector pointing in the x direction, and α is the Gaussian thermostatting multiplier. The above set of equations is solved using an operator splitting technique.[56] This method ensures a homogeneous shear field and a constant temperature within the whole simulation box. Thus, arbitrarily high shear rates may be established without the need for considering any effects of temperature gradients on the viscosity, making this method well suited for studies at high shear rates.

Near equilibrium (small γ) shear viscosity values have been obtained using both techniques. In the case of the reverse MD method this is done at low shear rates, where dv_x/dy is nearly uniform between slabs A and B. We calculate $\eta_{\rm eq}$ from

$$|j_y| = \eta_{\rm eq} \frac{dv_x(y)}{dy} = \frac{\Delta p}{2t_{\rm sim} L_y}, \tag{15}$$

where Δp is the total x-directional momentum exchanged between slabs A and B during the whole simulation time $t_{\rm sim}$.[54] In the homogeneous shear algorithm the off-diagonal element of the pressure tensor is measured during the course of the simulation, just like in the case of an equilibrium simulation (see Eq. (12)), and the shear viscosity is obtained as[55]:

$$\eta = \lim_{t\to\infty} \frac{-\langle P^{xy}(t)\rangle}{\gamma}. \tag{16}$$

As illustrations, Fig. 8 shows the $v_x(y)$ velocity profiles established using the reverse MD method, while Fig. 9 shows particle trajectories using the homogeneous shear algorithm.

Our results for $\eta_{\rm eq}$ as a function of Γ, for different values of κ are plotted in Fig. 10(a). Here we include results not only from the non-equilibrium simulations, but also from the two equilibrium simulations. We find excellent agreement among all the simulations in the value of the viscosity and the shape of its curve. A prominent feature of the viscosity of the present system is a minimum (e.g. at $\Gamma \cong 20$ for $\kappa = 1$), which was familiar for 3D Coulomb and Yukawa liquids, and which we also saw in the 2D dusty plasma experiment reviewed above. The shape of the $\eta_{\rm eq}(\Gamma)$ curve can be explained by the prevailing kinetic and potential contributions to the viscosity at low and high values of Γ, respectively, similarly to their 3D counterparts.

Similarly to the case of 3D Yukawa liquids as found by Saigo and Hamaguchi,[33] we observe that the near-equilibrium viscosity $\eta_{\rm eq}$ obeys a scaling law as demonstrated in Fig. 10(b), where the viscosity has been normalized by the Einstein frequency $\eta_{\rm E} = mn\omega_{\rm E}a^2$. Since $\omega_{\rm E}$ depends on κ, it was necessary for us to compute $\omega_{\rm E}(\kappa)$ with Eq. (7) of Kalman *et al.*[57] using pair-correlation functions measured from our simulations. The horizontal axis is the normalized temperature $T' = T_y/T_m = \Gamma_m/\Gamma$, where T_m and Γ_m are melting-point values reported by Hartmann *et al.*[16] Using these normalizations, the data fall on the same curve,

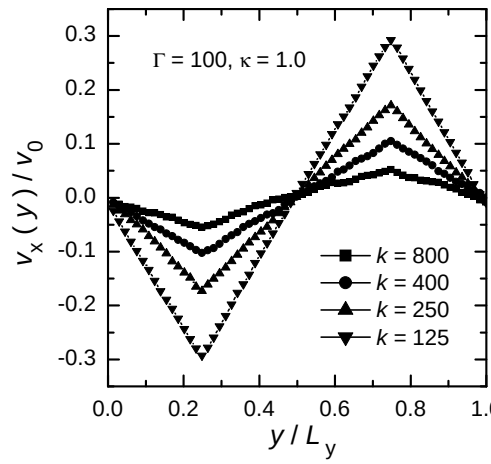

Fig. 8. Velocity profiles building up in the system in the reverse MD method at different rates of exchange of momentum between slabs A and B, see Fig. 7(a). (k is the number of time steps between consecutive momentum exchanges.) Here, $\Gamma = 100$, $\kappa = 1$. The profiles are very nearly linear and scale with the frequency of momentum exchange.

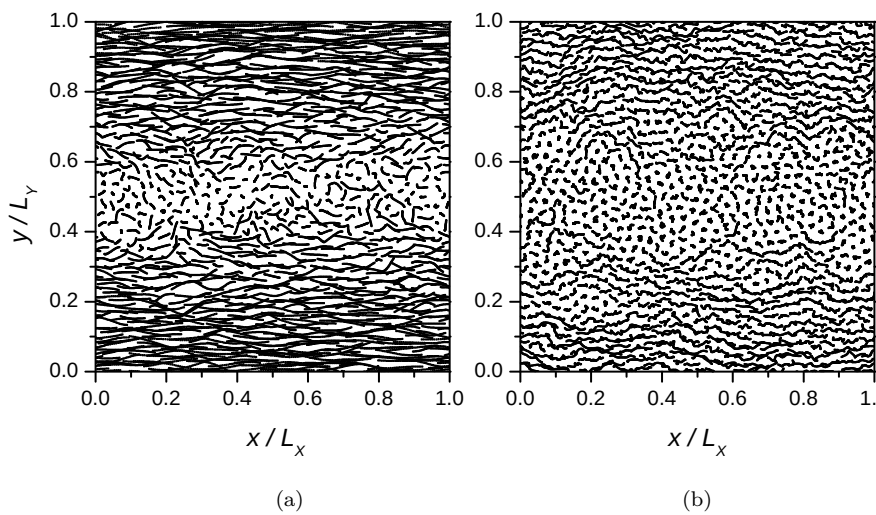

Fig. 9. Particle trajectories in the homogeneous shear algorithm, see Fig. 7(b), for normalized shear rates (a) $\bar{\gamma} = 0.2$ (time of recording: $\omega_0 \Delta t = 5.0$) and (b) $\bar{\gamma} = 0.05$ ($\omega_0 \Delta t = 23.6$), at $\Gamma = 100$, $\kappa = 1$. (Adapted from Ref. 53. Copyright (2006) by the American Physical Society.)

demonstrating the existence of a scaling law for the $0.5 \leq \kappa \leq 2.0$ range of the screening parameter. The near-equilibrium viscosity is fit by an empirical form

$$\frac{\eta_{\rm eq}}{\eta_{\rm E}} = aT' + \frac{b}{T'} + c \tag{17}$$

with coefficients: $a = 0.0093$, $b = 0.78$ and $c = 0.098$.

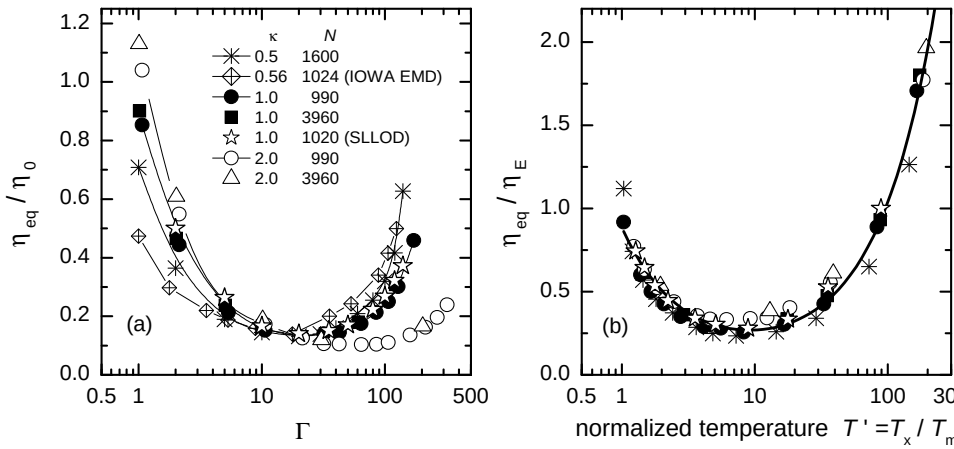

Fig. 10. (a) Small shear rate ("equilibrium") viscosity of the 2D Yukawa liquid, as a function of Γ, obtained from the reverse MD method using N = 990 and 3960 particles. SLLOD denotes the results of homogeneous shear method, and IOWA MD shows previous results obtained from equilibrium EMD simulations of Liu and Goree.[51] η is normalized by $\eta_0 = mn\omega_0 a^2$. (b) A scaling law for the shear viscosity. η is normalized by $\eta_{\rm E} = mn\omega_{\rm E} a^2$. (Adapted from Ref. 53. Copyright (2006) by the American Physical Society.)

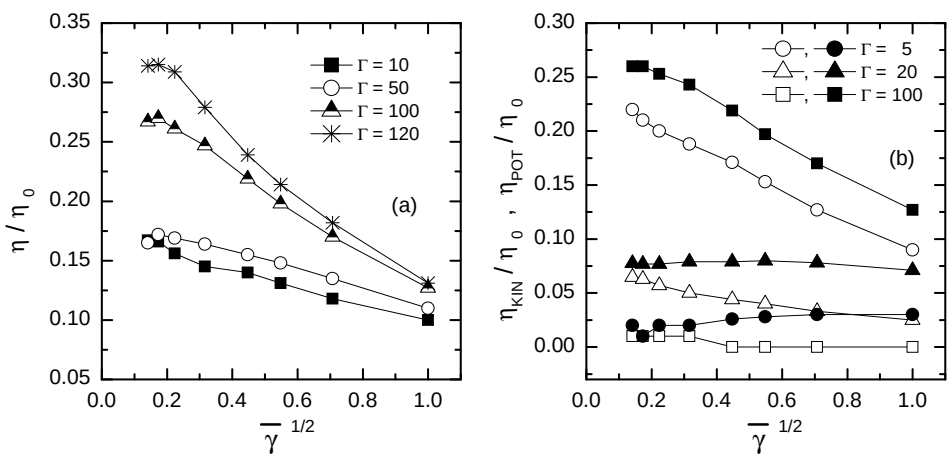

Fig. 11. (a) Dependence of shear viscosity on the normalized shear rate $\bar{\gamma}$, as obtained from the homogeneous shear method. Kinetic (open symbols) and potential (filled symbols) contributions to η as a function of $\bar{\gamma}$. (Adapted from Ref. 53. Copyright (2006) by the American Physical Society.)

A shear-thinning effect is revealed in Fig. 11(a), which shows that η decreases significantly as the shear rate $\overline{\gamma}$ is increased. In other two-dimensional systems the reduction in η, as compared to the value at small shear, was observed to vary as the square root of $\overline{\gamma}$.[19] We find that this scaling also occurs for the Yukawa system, as indicated by data that fall nearly on a straight line in Fig. 11(a) for $\overline{\gamma} > 0.2$. At smaller shear rates, $\overline{\gamma} < 0.2$, however, the shear thinning effect is less pronounced

and the liquid is more nearly Newtonian, especially for large Γ. Results are shown for $\overline{\gamma} \gtrsim 0.01$, which we found to be reliable, whereas at lower $\overline{\gamma}$ the homogeneous shear method yielded noisy data even for very long simulations.

Because viscosity arises from both kinetic and potential contributions, we identify in Fig. 11(b), which of these contributions is responsible for shear-thinning. Recall that for equilibrium conditions, the kinetic term dominates for $\Gamma \ll 20$ and the potential term dominates for $\Gamma \gg 20$. In Ref. 53 we find that for non-equilibrium conditions, as the shear rate increases, the reduction in viscosity is mostly due to a reduction of the kinetic contribution, except for Γ above the minimum.

We now compare the experimental and simulation results for viscosity as a function of Γ. The data, Figs. 5(b) and 10(a) for experiment and simulation, respectively, have the same normalizations. They exhibit a number of similarities, but are not in complete agreement. Both the experiment and simulation exhibit the minimum in the viscosity that we have often mentioned in this review paper. This minimum is different from the case of molecular liquids which have a viscosity that diminishes monotonically with increasing temperature. The value of the viscosity at the minimum is in agreement, within the error bars shown in Fig. 3 of Ref. 51. The most significant difference is that the minimum in the experimental Fig. 5(b) is much broader, and is located at a much higher Γ, than for the simulation. The reason for this difference is not yet certain, but there are at least three possibilities. First, in the experiment there was a shear, and moreover this shear was not varied independently of Γ, so that there is a possibility that shear thinning complicates the interpretation of the experimental results. Two additional explanations, which were suggested in Ref. 51, arise from inhomogeneity and anisotropy in the experiment that are lacking in the simulation. First, the experiment had an applied shear that had a specific scale length and that was in a specific direction. In contrast, the simulation was in equilibrium, with the shear corresponding to thermal motions that had a wide range of length scales including very short length scales, and the direction of the shear fluctuated isotropically. Second, the experiment had a non-uniform temperature; therefore it had non-uniform values of Γ and η whereas the simulation was uniform. The values reported for η and Γ in the experiment were computed as spatial averages over a region that had a non-uniform temperature. This non-uniformity could possibly be eliminated in a future experiment using a different heating scheme.

5. Summary

This paper intended to review experimental and numerical simulation work aimed at the determination of the shear viscosity of two-dimensional Yukawa liquids.

In the experiment of Nosenko and Goree,[37] reviewed in Sec. 3, the shear viscosity in a 2D dusty plasma layer was determined by measuring a sheared velocity profile produced using two counterpropagating laser beams and by fitting this profile to the solution of the Navier–Stokes equation. The experiment has successfully been simulated by molecular dynamics technique, as described in Sec. 4.1.

Both equilibrium and non-equilibrium molecular dynamics simulations have been used for the calculation of the shear viscosity on idealized 2D Yukawa liquids where friction terms arising from the interaction of the dust particles and the plasma have been neglected (Secs. 4.2 and 4.3). We have found reasonable agreement between the results of equilibrium[51] and non-equilibrium simulations in the limit of small shear rates. The two non-equilibrium approaches (the reverse molecular dynamics method and the homogeneous shear algorithm) used by us[53] presented data which were in excellent agreement with each other in this limit. By applying the homogeneous shear algorithm of Evans and Morriss[55] we observed a decrease in the shear viscosity of the 2D Yukawa liquid (*shear thinning*) with increasing shear rate.

Acknowledgments

This work has been supported by the Hungarian Scientific Research Fund through the grants OTKA-T-48389, OTKA-IN-69892, OTKA-PD-049991 and MTA-OTKA 90/46140. JG was supported by NASA and DOE.

References

1. G. J. Kalman, K. B. Blagoev and M. Rommel (eds.), *Strongly Coupled Coulomb Systems* (Plenum Press, 1998).
2. A. Melzer, V. A. Schweigert, I. V. Schweigert, A. Homann, A. Peters and A. Piel, *Phys. Rev. E* **54** (1996) R46.
3. J. B. Pieper, J. Goree and R. A. Quinn, *J. Vac. Sci. Technol. A* **14** (1996) 519.
4. M. Zuzic, A. V. Ivlev, J. Goree *et al.*, *Phys. Rev. Lett.* **85** (2000) 4064.
5. S. Robertson, A. A. S. Gulbis, J. Collwell and M. Horányi, *Phys. Plasmas* **10** (2003) 3874.
6. Z. Sternovsky, M. Lampe and S. Robertson, *IEEE Trans. Plasma Sci.* **32** (2004) 632.
7. H. Löwen, E. Allahyarov, C. N. Likos, R. Blaak, J. Dzubiella, A. Jusufi, N. Hoffmann and H. M. Harreis, *J. Phys. A* **36** (2003) 5827.
8. H. Löwen, J.-P. Hansen and J.-N. Roux, *Phys. Rev. A* **44** (1991) 1169.
9. A. P. Hynninen and M. Dijkstra, *J. Phys. Condens. Matter* **15** (2003) S3557.
10. S. Auer and D. Frenkel, *J. Phys. Condens. Matter* **14** (2002) 7667.
11. W. L. Slattery, G. D. Doolenn and H. E. DeWitt, *Phys. Rev. A* **26** (1982) 2255.
12. R. T. Farouki and S. Hamaguchi, *Phys. Rev. E* **47** (1993) 4330.
13. S. Muto and H. Aoki, *Phys. Rev. B* **59** (1999) 14911.
14. R. C. Gann, S. Chakravarty and G. V. Chester, *Phys. Rev. B* **20** (1979) 326.
15. S. Hamaguchi, R. T. Farouki and D. H. E. Dubin, *Phys. Rev. E* **56** (1997) 4671.
16. P. Hartmann, G. J. Kalman, Z. Donkó and K. Kutasi, *Phys. Rev. E* **72** (2005) 026409.
17. P. Hartmann, Z. Donkó, P. M. Bakshi, G. J. Kalman and S. Kyrkos, *IEEE Trans. Plasma Sci.* **35** (2007) 332.
18. R. L. Merlino and J. A. Goree, *Physics Today* **57** (2004) 32.
19. D. J. Evans, *Phys. Rev. A* **23** (1981) 1988.
20. A. Kabla and G. Debregeas, *Phys. Rev. Lett.* **90** (2003) 258303; J. B. Salmon, A. Colin, S. Manneville, and F. Molino, *ibid.* **90** (2003) 228303; F. Varnik, L. Bocquet, J.-L. Barrat, and L. Berthier, *ibid.* **90** (2003) 095702; Y. Jiang *et al.*, *Phys. Rev. E* **59** (1999) 5819.

21. C.-L. Chan, W.-Y. Woon and L. I, *Phys. Rev. Lett.* **93** (2004) 220602.
22. A. V. Ivlev, V. Steinberg, R. Kompaneets, H. Höfner, I. Sidorenko and G. E. Morfill, *Phys. Rev. Lett.* **98** (2007) 145003.
23. K. Y. Sanbonmatsu and M. S. Murillo, *Phys. Rev. Lett.* **86** (2001) 1215.
24. P. Vieillefosse and J. P. Hansen, *Phys. Rev. A* **12** (1975) 1106.
25. J. Wallenborn and M. Baus, *Phys. Lett.* **61A** (1977) 35.
26. J. Wallenborn and M. Baus, *Phys. Rev. A* **18** (1978) 1737.
27. B. Bernu, P. Vieillefosse and J. P. Hansen, *Phys. Lett.* **63A** (1977) 301.
28. B. Bernu and P. Vieillefosse, *Phys. Rev. A* **18** (1978) 2345.
29. Z. Donkó and B. Nyíri, *Phys. Plasmas* **7** (2000) 45.
30. S. Bastea, *Phys. Rev. E* **71** (2005) 056405.
31. J. Daligault, *Phys. Rev. Lett* **96** (2006) 065003.
32. G. Salin and J.-M. Caillol, *Phys. Rev. Lett.* **88** (2002) 065002; *Phys. Plasmas* **10** (2003) 1220.
33. T. Saigo and S. Hamaguchi, *Phys. Plasmas* **9** (2002) 1210.
34. M. S. Murillo, *Phys. Rev. E* **62** (2000) 4115.
35. G. Faussurier and M. S. Murillo, *Phys. Rev. E* **67** (2003) 046404.
36. P. Bakshi, Z. Donkó and G. J. Kalman, *Contrib. Plasma Phys.* **43** (2003) 261.
37. V. Nosenko and J. Goree, *Phys. Rev. Lett.* **93** (2004) 155004.
38. B. Liu, J. Goree, V. Nosenko and L. Boufendi, *Phys. Plasmas* **10** (2003) 9.
39. U. Konopka, G. E. Morfill and L. Ratke, *Phys. Rev. Lett.* **84** (2000) 891.
40. G. E. Morfill, M. Rubin-Zuzic, H. Rothermel, A. V. Ivlev, B. A. Klumov, H. M. Thomas, U. Konopka and V. Steinberg, *Phys. Rev. Lett.* **92** (2004) 175004.
41. D. Frenkel and B. Smit, *Understanding Molecular Dynamics Simulations* (Academic Press, 2001).
42. P. P. Ewald, *Ann. Phys.* **64** (1921) 253.
43. J. W. Eastwood, R. W. Hockney and D. N. Lawrence, *Comput. Phys. Commun.* **19** (1980) 215.
44. C. Sagui and T. A. Darden, *Ann. Rev. Biophys. Biomol. Struct.* **28** (1999) 155.
45. N. David and S. M. Hooker, *Phys. Rev. E* **68** (2003) 056401.
46. R. Gargallo, P. H. Hünenberger, F. X. Avilés and B. Oliva, *Protein Science* **12** (2003) 2161.
47. N. David, D. J. Spence and S. M. Hooker, *Phys. Rev. E* **70** (2004) 056411.
48. J.-P. Hansen and I. R. McDonald, *Theory of Simple Liquids* (Academic Press, 1976).
49. B. J. Alder and T. E. Wainwright, *Phys. Rev. A* **1** (1970) 18.
50. M. H. Ernst, E. H. Hauge and J. M. J. van Leeuwen, *Phys. Rev. Lett.* **25** (1970) 1254.
51. B. Liu and J. Goree, *Phys. Rev. Lett.* **94** (2005) 185002.
52. Z. Donkó, J. Goree, P. Hartmann and Bin Liu, to be published.
53. Z. Donkó, J. Goree, P. Hartmann and K. Kutasi, *Phys. Rev. Lett.* **96** (2006) 145003.
54. F. Müller-Plathe, *Phys. Rev. E* **59** (1999) 4894.
55. D. J. Evans and G. P. Morriss, *Statistical Mechanics of Nonequilibrium Liquids* (Academic Press, 1990).
56. G. Pan, J. F. Ely, C. McCabe and D. J. Isbister *J. Chem. Phys.* **122** (2005) 094114.
57. G. J. Kalman, P. Hartmann, Z. Donkó and M. Rosenberg, *Phys. Rev. Lett.* **92** (2004) 065001.